# International Conference on Space Optics—ICSO 2018

Chania, Greece

9–12 October 2018

*Edited by Zoran Sodnik, Nikos Karafolas, and Bruno Cugny*

# *Manufacturing and optical performance of silicon immersed gratings for Sentinel-5*

*Ralf Kohlhaas*

*Paul Tol*

*Ruud Schuurhof*

*Robert Huisman*

*et al.*

esa icso proceedings cnes

International Conference on Space Optics — ICSO 2018, edited by Zoran Sodnik, Nikos Karafolas, Bruno Cugny, Proc. of SPIE Vol. 11180, 111801L · © 2018 ESA and CNES · CCC code: 0277-786X/18/$18 · doi: 10.1117/12.2535976

# Manufacturing and optical performance of silicon immersed gratings for Sentinel-5

Ralf Kohlhaas*, Paul Tol, Ruud Schuurhof, Robert Huisman, Stephen J. C. Yates, Geert Keizer, René Wanders, Sander van Loon, Tonny Coppens, Mustafa Kaykisiz, Phillip Laubert, Peter Paul Kooijman, Aaldert van Amerongen, Luc Dubbeldam

SRON Netherlands Institute for Space Research, Sorbonnelaan 2, 3584 CA Utrecht, Netherlands

## ABSTRACT

In this article the immersed gratings for the ESA Copernicus Sentinel-5 mission are presented. The manufacturing approach is shown and the optical performance of the SWIR-3 immersed gratings as well as the results of the environmental tests are discussed. The immersed gratings show an average efficiency of 60% and a wavefront error of 200 nm rms. The total integrated scatter over the complete stray-light hemisphere excluding ghosts from internal reflections is found to be 0.2% using a conservative estimate. A method for the derivation of the wavefront error from separate surface measurements is presented and the results are compared to measurements with an experimental Shack-Hartmann setup. The immersed gratings are produced by bonding a prism to a wafer with a grating. Environmental tests and testing at operational temperatures show the suitability of this approach for complex space optical components. The article concludes with possible improvements in the optical performance of future immersed gratings.

**Keywords:** immersed grating, Sentinel-5, silicon, short-wave infrared, stray light, wavefront error, efficiency, Lyman ghosts

## 1. INTRODUCTION

In 1822, Joseph van Fraunhofer realized that a grating immersed in a medium of refractive index $n$ will receive an increase in its resolving power by the factor of the refractive index[1]. This enables grating spectrometers with the same resolving power but a much smaller size, depending on the spectrometer design with a reduction factor of up to $n^3$. Instead of a liquid as in typical immersion microscopes, solid prisms with high refractive index materials as the immersive medium offer an attractive design option. Such immersed gratings have been developed for ground-based astronomy, most notably by the groups of D. T. Jaffe[2] and P. J. Kuzmenko[3] and recently by Canon[4]. The size reduction of imaging spectrometers using immersed gratings is of strong interest for space optical instruments. The TROPOMI instrument on board the ESA Copernicus Sentinel-5 Precursor satellite[5], launched in 2017, contains a silicon immersed grating that was jointly developed and patented by TNO and SRON[6,7]. This is the first use of an immersed grating in space.

The immersed gratings of the Sentinel-5 mission are provided by SRON as well. Airbus Defense and Space is the prime contractor for Sentinel-5 and the immersed gratings are integrated into the short-wave infrared (SWIR) spectrometer[8] of Leonardo. For TROPOMI the immersed grating was produced by direct lithography on a silicon cylinder and subsequent cutting out of a prism shape. In order to cope with the tighter requirements for Sentinel-5, the manufacturing approach was updated and based instead on the direct bonding of a thin silicon grating element with a silicon prism. This made it possible to control the prism and grating-surface performances separately. The strategy was first demonstrated in an internal development project at SRON[9] and the results for the Sentinel-5 immersed gratings are presented here in detail.

Immersed gratings were produced for the three satellites of the Sentinel-5 mission containing each an immersed grating for the SWIR-1 spectral range (1589 nm – 1676 nm) and the SWIR-3 spectral range (2304 nm – 2386 nm). Flight spares and three additional SWIR-3 immersed gratings (Bread Board Model, Qualification Model, Engineering Model) were manufactured for testing and integration in a spectrometer demonstrator model, bringing the total number of immersed gratings to 11. Performance testing was so far only performed on the additional SWIR-3 immersed gratings and all performance results presented here are based on those models. In Section 2 of this article the optical design of the immersed gratings is presented. The manufacturing of the immersed gratings is described in Section 3 and in Section 4 the results of optimal performance tests at room temperature are presented. In Section 5 the environmental tests on the

immersed gratings integrated in a housing are shown. We conclude in Section 6 with a summary of the performance results and discuss possible future improvements of the immersed gratings.

## 2. OPTICAL DESIGN

The design of the immersed gratings for SWIR-1 and SWIR-3 is shown in Figure 1. Light passes from the left through an antireflection-coated entrance surface, travels through silicon ($n \approx 3.4$), is diffracted at an aluminum-coated blazed grating surface, and leaves again through the entrance surface. Only the main diffraction order can leave the immersed grating directly, whereas light from spurious orders is reflected back into the immersed gratings by total internal reflection. The designs were optimized in order to avoid any ghosts from internal reflections within the relevant spectrometer detector range (spectral field of view) of about 20°. This led to the choice of a tilted entrance surface. An absorption coating was applied on the third surface to reduce further the intensity of ghosts from internal reflections.

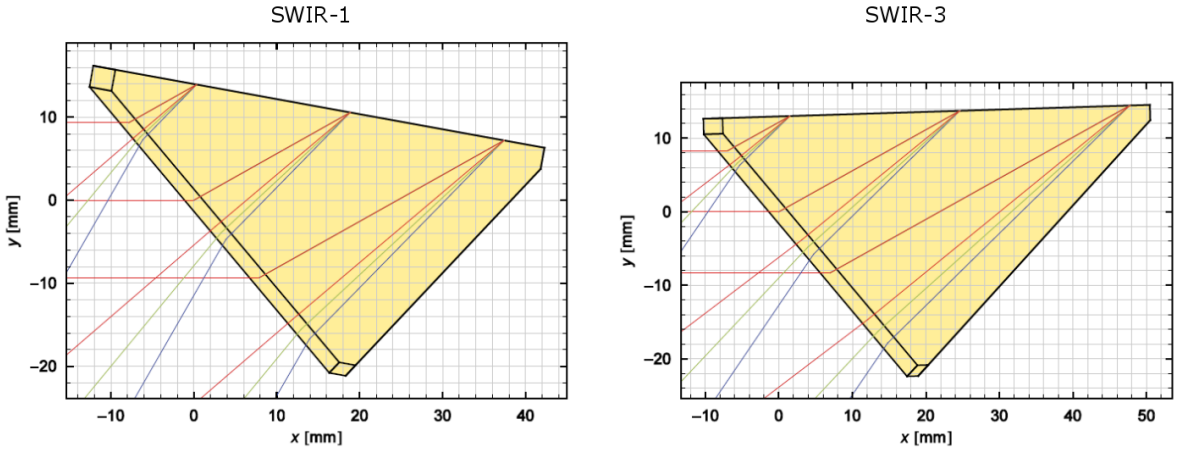


Figure 1. Optical design of immersed gratings for Sentinel-5 for the SWIR-1 channel (left) and for SWIR-3 (right). The incoming beam is shown in red and the diffracted beams in red, green and blue with decreasing wavelengths. The grating surface contains a blazed grating (not shown).

The grating period was chosen to be 2070 nm. Details on the blazed grating surface are given in Section 3.1. The SWIR-1 immersed gratings are operated in order 6 and the SWIR-3 immersed gratings in order 5. The dispersion is in of the range 217°/µm – 221°/µm for SWIR-1 and in of the range 215°/µm – 231°/µm for SWIR-3. The efficiency was required to be at least 59% in SWIR-1 and 55% in SWIR-3. One SWIR-3 immersed grating can be seen in Figure 2, here in the inset of a storage container.

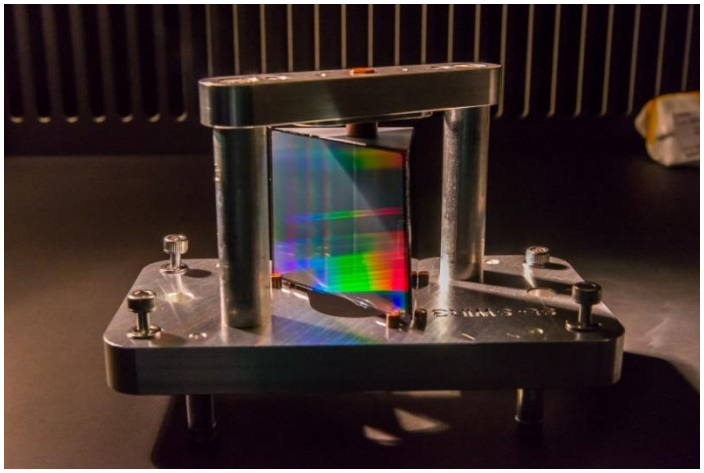

Figure 2. SWIR-3 immersed grating in a storage container inset.

# 3. MANUFACTURING

## 3.1 General manufacturing flow

Immersed gratings for Sentinel-5 were produced by the direct bonding of a silicon wafer containing the blazed grating to a silicon prism as illustrated in Figure 3. After bonding and fusing of the grating element, excess wafer parts were removed with a scribe and break method and coatings on all immersed grating surfaces were applied. Silicon prisms were procured at Thales SESO in France and the grating element manufacturing took place at the facilities of Phillips Innovation Services with SRON staff. The separate production of prisms and grating elements allowed us on the one hand to keep the stringent dimensional and performance requirements on the prisms (angular tolerance 1'30", surface shape errors <10 nm rms, roughness <0.5 nm rms, low number of digs and scratches) while on the other hand the grating element could be produced and optimized with standard lithographic equipment. The best grating elements and prisms were then chosen for the immersed grating bonding. In the following sections, details on the immersed grating production process are presented, with a focus on grating element manufacturing and bonding.

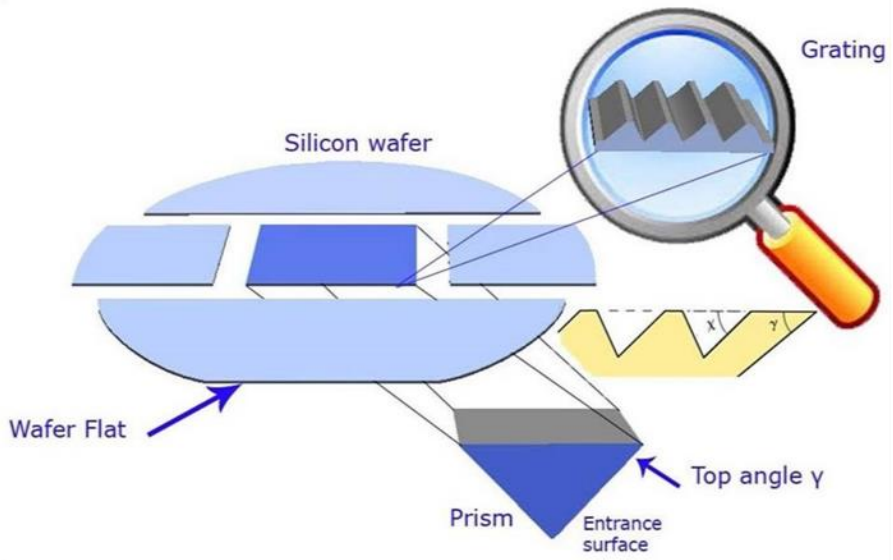


Figure 3. Schematic representation of the main immersed grating components. A silicon wafer with a grating structure is bonded to a silicon prism and excess wafer parts are removed after bonding.

## 3.2 Grating element manufacturing

The design of the grating profiles for SWIR-1 and SWIR-3 can be seen in Figure 4. The blaze angles were 44.5° for SWIR-1 and 56° for SWIR-3. Since one groove angle was fixed to 70.5 degrees by the intersection of the (111) crystal planes used for KOH etching, the blaze angle was set by off-cut angles of 10.24° and 1.26° versus the (100) crystal plane. The period of 2070 nm was set in practice by the period of the grating mask. The small dam widths of 400 nm for SWIR-1 and 380 nm for SWIR-3 were the main challenges for the grating element manufacturing.

The grating elements were produced starting with 6 inch wafers polished on both sides. A standard UV lithography process was used as summarized in Figure 5. For the resist exposure a mask produced with direct writing UV lithography was used with a linewidth of 500 nm. The gratings have been etched with KOH taking advantage of the different etching rates in each Si lattice direction: the etch rate in the (100) direction is much faster than in the (111) direction. Because of this the (111) surface acts as an etch stop leading to a controlled etching process with a well-defined groove profile. The final grating elements for SWIR-3 have an average dam width of 380 nm within a range of ±16 nm and a standard deviation in the dam widths below 25 nm rms over a single wafer. The defect density was measured to be below 0.001% and therefore negligible as a stray-light contribution.

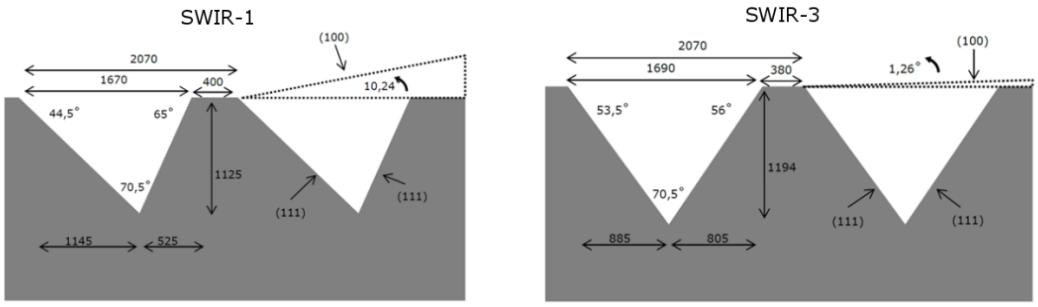


Figure 4. Grating profiles for SWIR-1 (left) and SWIR-3 (right). All distances are in nm.

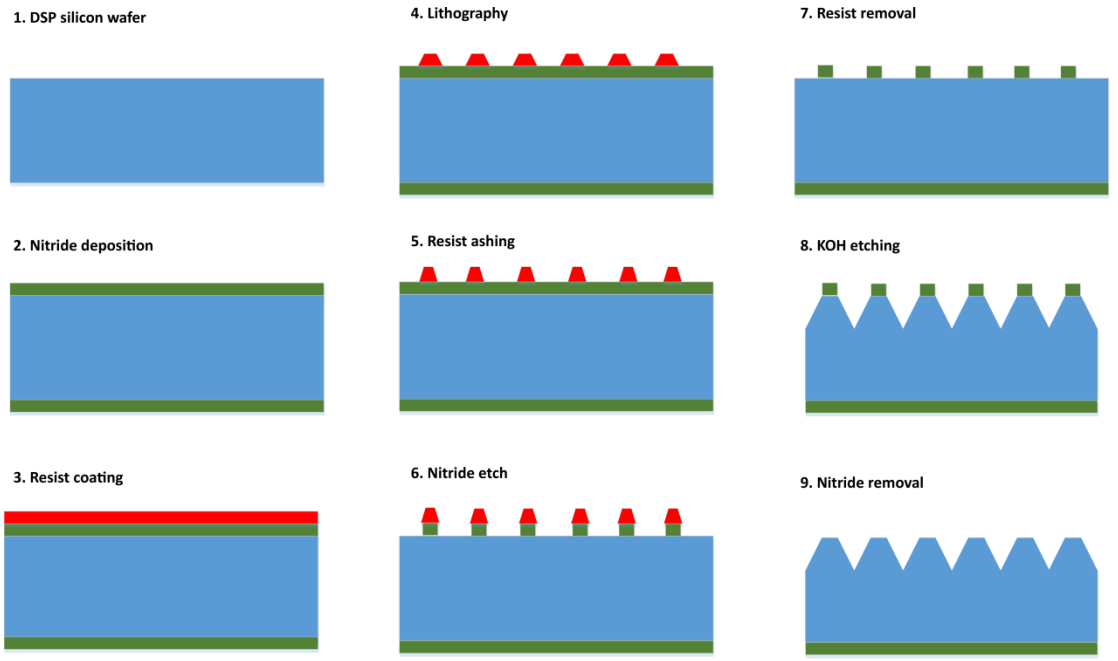


Figure 5. Grating element manufacturing flow.

For the etching a precise alignment of the grating mask with the Si lattice was required. Because the wafer flat was not accurate enough for this purpose, a Vangbo alignment structure has been etched prior to patterning the gratings. In this way an accuracy of better than 0.05° was reached. This results in a very smooth grating-groove surface close to the atomic lattice profile. A top view SEM image and Vangbo pattern are shown in Figure 6.

Finally a protection layer of $SiO_2$ was deposited on the grating surface to protect the grating from contamination and damage during the next process steps. This layer was removed just before aluminum deposition on the grating surface.

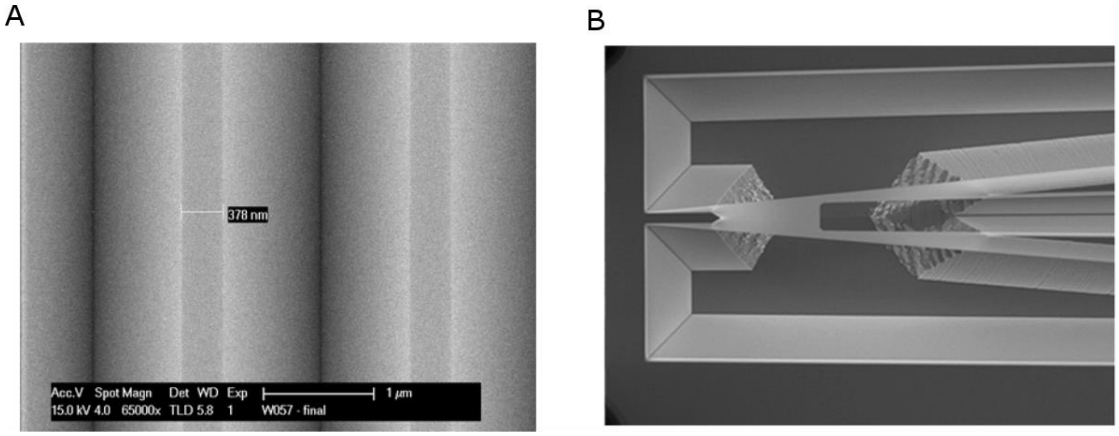


Figure 6. A: Top view of SWIR-3 grating element with indication of the dam width. B: Vangbo pattern for grating wafer orientation.

### 3.3 Bonding

Prisms and grating elements were bonded by direct contact bonding and subsequent thermal fusing. In direct hydrophilic contact bonding of silicon, two activated surfaces of low surface roughness are pressed against each other forming Si-O-Si bonds. The silicon surfaces were prepared before bonding with a thorough cleaning of the prism and wafer surfaces and subsequent plasma activation to form Si-OH on the surfaces. After bonding a fusing step was used to remove remaining OH groups to strengthen the atomic bonds between the surfaces.

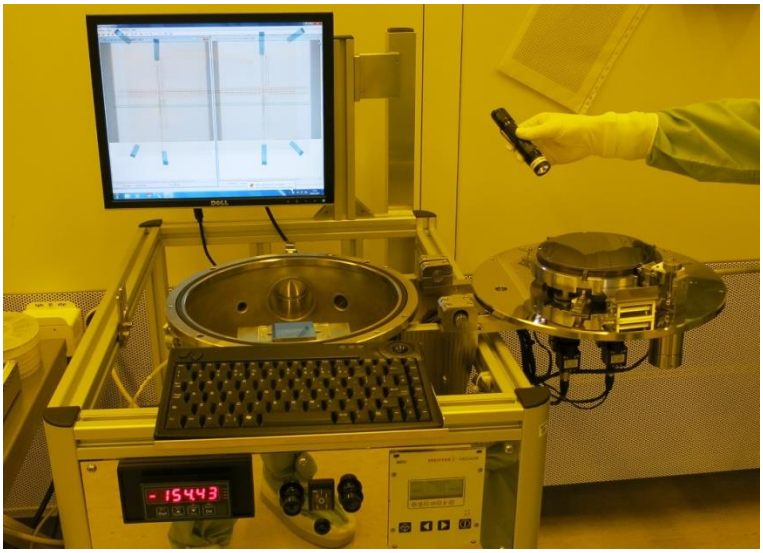


Figure 7. Wafer bonder from AML, modified for prism to wafer bonding. The prism sits at the center of the bonder chamber and the wafer is clamped in the bonder lid. Two infrared cameras record the wafer alignment through holes in the lid.

For the bonding of prisms and wafers a modified wafer bonder from AML was used as shown in Figure 7. The prism was set in the center of the bonding chamber in a prism support and the wafer was clamped in the lid of the bonder. During the bonding a spring pin in the middle of the wafer bent the wafer and the lower plate of the bonder was elevated in order to press the prism against the wafer. It was found that the prism to wafer bonding is considerably more challenging than standard wafer to wafer bonding. A strictly timed and structured substrate cleaning and bonding procedure was needed. In addition, the prism and wafer had to be made equidistant to a high degree in the preparation of the bonding. As a first step, the upper and lower plates of the bonder were measured and set equidistant. The prism was placed in the prism support and its orientation with respect to the support was measured with a coordinate measuring machine (CMM). Differences were then corrected with actuators on the lower plate of the bonder. All mechanical preparatory steps were taken before the cleaning of the substrates.

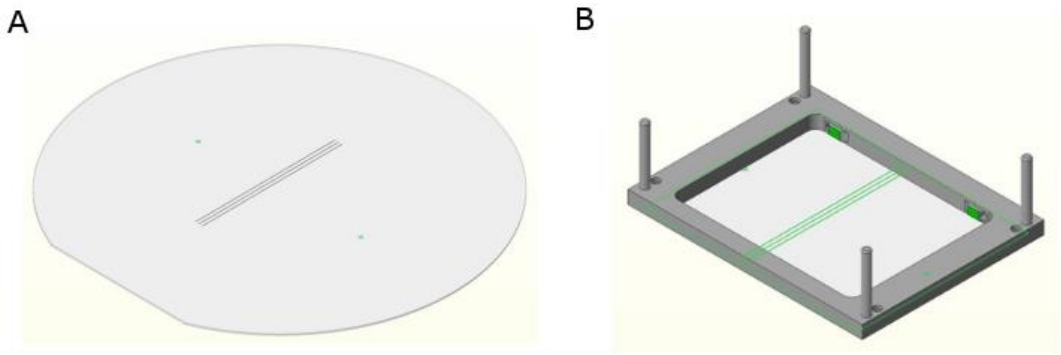


Figure 8. A: Illustration of wafer with alignment marks. On the actual grating elements, grating lines were present over the complete wafer except on the fields of the alignment marks. B: Alignment tool including a spare grating element, which was connected to the prism support.

Another challenge in bonding was to align the triangular prism surfaces and the grating lines perpendicular within a required maximum deviation of 6 arcminutes. To align the prism with the alignment marks on the wafer (see Figure 8), two cameras looking through holes in the lid of the bonder were used. On the prism support a removable alignment tool was placed that included a spare grating element to provide alignment marks for the prism. The orientation of the prism relative to the wafer was measured in vacuum and at room pressure and the difference was taken into account in the alignment. Furthermore, a rotation stabilization system was added to the bonder to ensure that during elevation of the lower bonder plate no rotational errors were added. The alignment after bonding was verified with a specially designed setup shown in Figure 9. The edge of an aluminum plate was brought into contact with a triangular side of the prism using mechanical pressure. Another plate with a parallel edge hovered over the alignment marks on the bonded grating element. Via a microscope the distances between the alignment marks and the plate edge were measured in order to determine the rotation. The grating lines in all flight models were verified to be perpendicular to the triangular prism sides within 100 arcseconds.

After fusing, all immersed gratings were checked with an infrared camera and shown to be free of voids between the prism and grating element. Excess wafer parts were removed using a diamond scribe on the prism wafer edges and subsequent braking of the overhanging wafer parts. After scribe and break, a wafer overhang of at most 0.5 mm over the prism remained. Alignment marks as in the rotational alignment and verification were located in the excess wafer parts and were therefore not part of the final grating surface.

Figure 9. Setup for verification whether the grating lines and the triangular prism surfaces are perpendicular. The bonded wafer is on top of the dark prism. The excess wafer parts are not yet removed. Above and below the wafer are aluminum plates with parallel edges. A spring pushes the lower alignment plate against the prism side. The rotation is determined from the distances between the upper aluminum plate edge and the alignment marks on the bonded wafer.

### 3.4 Coatings

The grating surfaces of the immersed gratings were coated with a 500 nm aluminum layer protected with 150 nm $SiO_2$. Thickness variations of the coating were below 4 nm rms. The antireflection coatings on the entrance surfaces and

absorption coatings on the third surfaces were deposited by CILAS in France. The antireflection coatings have a reflectivity smaller than 0.2% over the complete spectral range. For the absorption coatings reflectivities below 1.5% were obtained. The performance of the antireflection coatings was verified in vacuum under cryogenic conditions. For all coatings, samples underwent damp heat (relative humidity 85% at 60 °C during 7.5 days) and abrasion and adhesion tests without degradation of performance.

## 4. OPTICAL PERFORMANCE TESTING

### 4.1 Stray light

#### 4.1.1 Setup

Stray-light testing has been performed at the optical laboratory of ESA-ESTEC. For this purpose, the scatterometer setup was prepared and tested for the first time in the SWIR-3 wavelength range. A schematic representation of the stray-light setup and the used optomechanics is shown in Figure 10. A converging laser beam (light blue) leaves the beam preparation system (black box) and is sent on the immersed grating (in the black plastic enclosure) and reflected to a detector (red) at a distance of 0.5 m. The detector rotates in the horizontal plane around the immersed grating. During an angular scan, the aperture size at the detector is changed as a function of the angle from specular reflection in order to provide a large dynamic range of the measurement.

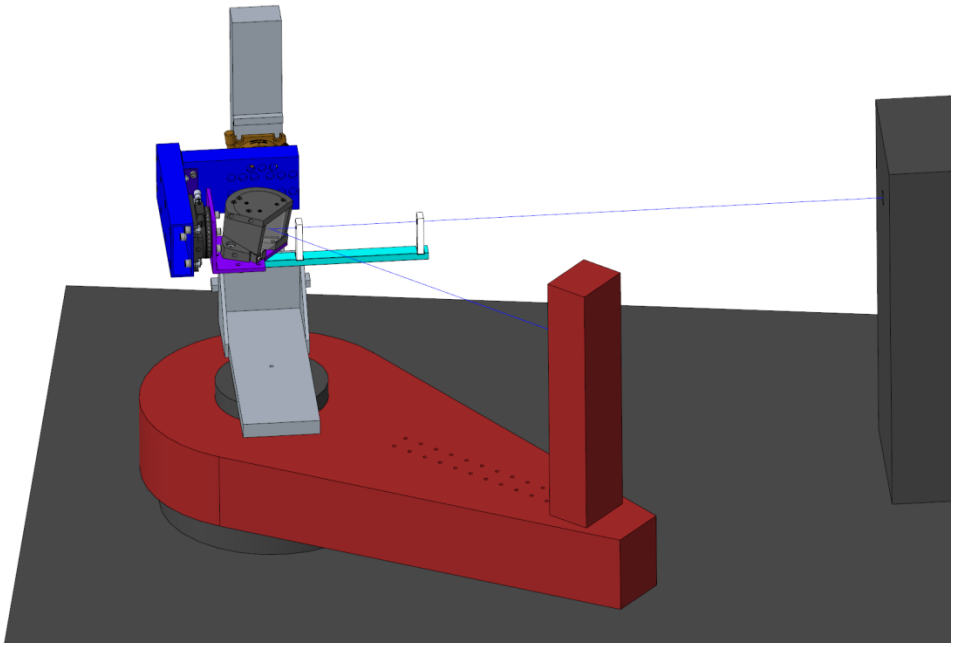

Figure 10. Schematic representation of the stray-light setup for the testing of the Sentinel-5 immersed gratings. The alignment rail (cyan) with two apertures (white) was removed during the stray-light measurement. The detector arm (red) rotates around the immersed grating during the measurement.

The initial alignment and preparation of the laser beam was performed with an alignment mirror placed on the mechanical interface platform (purple) instead of the immersed grating. The mirror was at the center of rotation of the detector and the mechanical interface, which was checked by rotating the optical setup. With the help of an alignment rail (cyan) with two apertures (white) the direction of the incident beam was confirmed. The enclosure of the immersed grating was used to correct for the wedged entrance surface of the immersed grating. It was placed on the platform such that the virtual intersection of incident and reflected beams was position at the center of the mirror. In this way, the mirror could simply be replaced by the immersed grating with only minor adjustments to the system. This alignment strategy can be generalized to any complex optical component in a stray-light setup.

Since the detector movement was constrained to the horizontal plane, only one-dimensional scans over the stray-light hemisphere could be performed for a given orientation of the immersed grating. Three configurations were used with the

immersed grating in spectral, spatial and off-axis spectral orientation (Figure 11). Due to the direct UV-beam writing process of the grating lithography mask, ghosts were expected in spectral and spatial direction due to periodic movements of the writing system perpendicular and along the grating lines. The off-axis measurement was taken to provide an estimate of the stray-light background. Figure 11 does not show peaks from internal reflections, which only exist outside of a range of 20° due to the immersed-grating design. Gaussian positioning errors of the grating lines can lead to a stray-light increase on the spectral and spatial axis with a smooth distribution as indicated by the slightly darker color along the two axes.

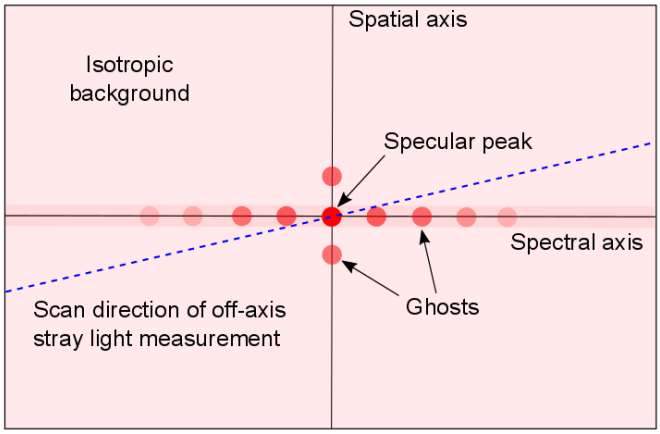


Figure 11. Illustration of the stray-light distribution and the axes for stray-light measurement in angular coordinates. Ghosts on the spectral and spatial axes are due to lithographic errors in the grating mask. The stray-light background is assumed to be centrosymmetric and quasi-isotropic. Ghosts from internal reflections are not depicted here, because they are by design outside the field of view of the detector in the Sentinel-5 SWIR spectrometer.

For the spectral orientation, the immersed grating was rotated such that the dispersion plane overlapped with the detector plane (this corresponds to the configuration shown in Figure 10). The measurement wavelength was set to 2377 nm and a bandpass filter was added to the system in order to suppress laser noise which would otherwise translate to stray light along the spectral axis. In order to check that the dispersion and detector planes were superimposed, the reflected-beam height was verified at a second wavelength. The spatial axis is perpendicular to the spectral axis. For the measurement the immersed grating was rotated by approximately 90° with the specular reflection 16° away from the incident beam. In the off-axis spectral configuration the immersed grating was rotated from the spectral configuration such that the spectral axis and horizontal axis formed an angle of 5°. Astigmatism introduced by the converging beam on the immersed grating was corrected in all measurement configurations by placing the circle of least confusion at the detector.

#### 4.1.2 Results

Stray-light results are expressed as the Bidirectional Reflectance Distribution Function (BRDF) defined as

$$\mathrm{BRDF}(\theta_s) = \frac{\Delta P_S(\theta_S)}{\Delta\Omega_S P_i \cos\theta_S},$$

with power $\Delta P_S$ scattered into a small solid angle $\Delta\Omega_S$, incident power $P_i$ and scatter angle $\theta_S$. The experimental BRDF results in spectral, spatial and off-axis spectral direction are shown in Figures 12 to 14.

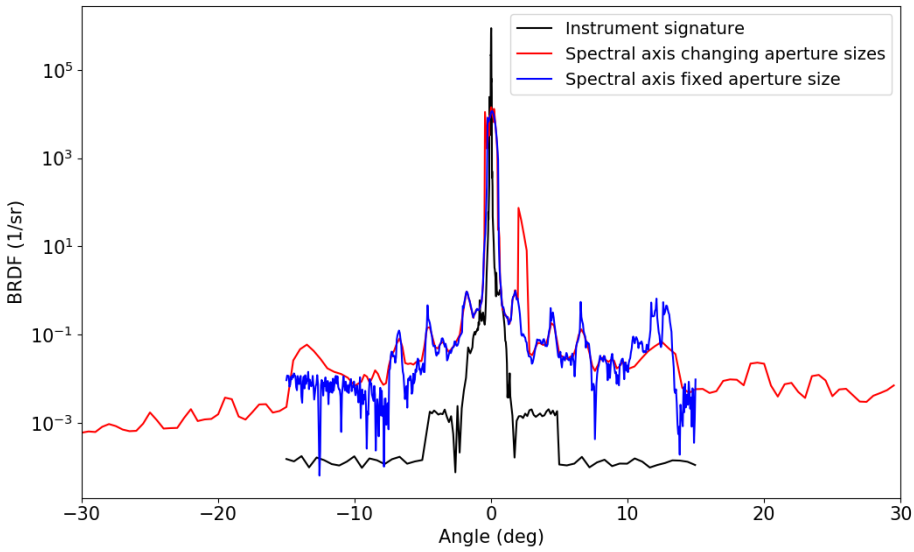


Figure 12. Measured stray light in the spectral direction as a function of angle from specular reflection (red) with the measurement in spectral direction with a fixed aperture size (blue). The instrument signature is shown in black. The larger peak at +2° in the red curve was a glitch during the measurement scan. Data shown here are from the SWIR-3 Engineering Model (EM).

In Figure 12, the spectral stray light as measured with the detector aperture size increasing from specular (red) or fixed (blue) are shown together with the instrument signature without the grating in the optical system (black). In comparison with the signature measurement, the peak intensity is reduced due to aberrations introduced by the converging beam on the immersed grating. The peaks in the stray-light spectrum are ghosts introduced by periodic errors in the grating mask of the lithographic process and have in general the same spatial dimension as the specular peak. The peaks at 1.7° can be translated to a spatial frequency of approximately 120 µm, which was a fundamental frequency in the mask-writing process perpendicular to the grating lines. The measurement with increasing aperture sizes at a larger angle from specular increases the dynamic range, but it has the risk of underestimating relative ghost intensities. An aperture size larger than the ghost size leads to an averaging with the stray-light background, effectively reducing BRDF values. For this reason, also a measurement with a fixed aperture size over a smaller angular range was performed (blue). It can be seen here that the ghosts are everywhere slightly higher in a region outside of ±2°. The maximum relative ghost intensity on the spectral axis estimated from the stray-light data is $8 \cdot 10^{-5}$ after correction for the small cosine obliquity factor in the BRDF definition.

In the spatial direction (Figure 13) the low stray-light background is only interrupted by ghosts at ±1.7°. This corresponds to a spatial frequency of approximately 80 µm, which was a fundamental frequency in the grating mask production process, here in the direction of the grating lines.

The results of the off-axis spectral measurement are shown in Figure 14. The off-axis stray-light results (red) are in a region of ±5° from specular still dominated by the contribution of the ghosts on the spectral axis. This was shown by a calculation using the data in spectral direction (blue) and the simulated point spread function (black) resulting in the calculated contribution to the off-axis stray light measurement (cyan) from the spectral axis. Outside of ±5° peaks at ±7° remain which were higher than expected from the calculation. This indicates that for these ghost peaks, the spatial extent is approximately 3 times larger than for the remaining ghosts on the spectral axis. The reason for this larger ghost size is unknown. Overall, all peaks found in the off-axis stray-light measurement could be attributed to contributions on the spectral axis, supporting the assumed stray-light distribution in Figure 11. This was further supported with a camera measurement of the SWIR-3 immersed grating at 1590 nm, where only ghosts on the spectral and spatial axes were found. For measurements with the SWIR-3 Flight Models (FMs) a larger off-axis angle will be used in order to reduce the contribution of the stray light on the spectral axis in the measurement.

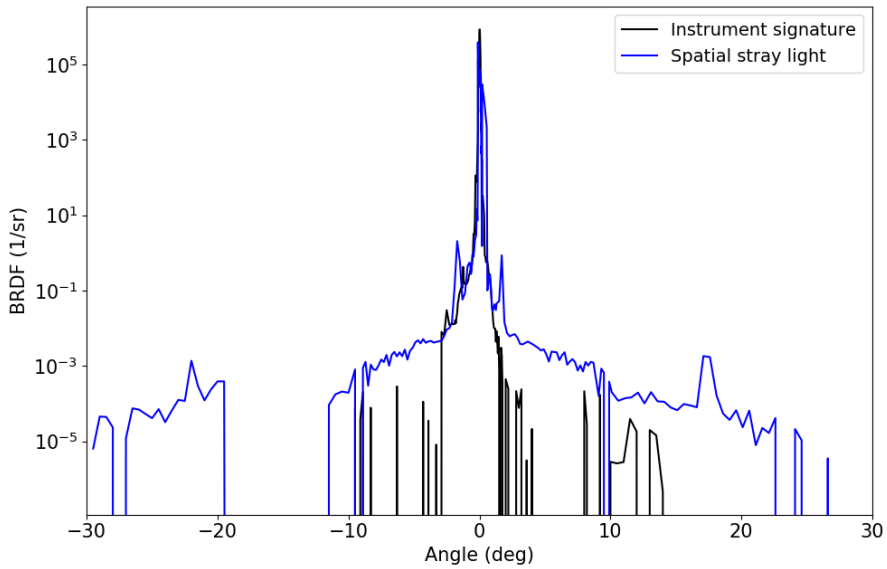


Figure 13. Measured stray light in the spatial direction as a function of angle from specular reflection (blue) and the instrument signature (black). The ghost at +17° is from the optomechanical interface of the stray-light setup while in the range from -12° to -20° no data is available due to the blocking of the incident laser beam by the detector. Data shown here are from the SWIR-3 Qualification Model (QM).

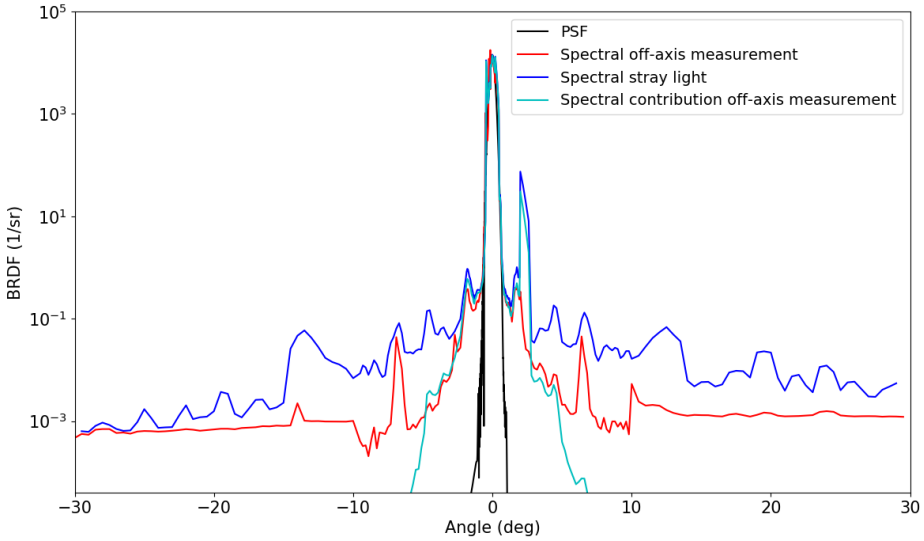


Figure 14. Spectral stray light (blue), simulated PSF (black), measured off-axis spectral stray light (red) and the calculated contribution from spectral stray light to the off-axis spectral measurement (cyan) using the PSF and the spectral measurement. Within a region of ±5° from specular the off-axis stray-light measurement was still dominated by the contribution from the spectral axis. No additional ghosts were found in the off-axis measurement. Data shown here are from the SWIR-3 EM.

With the goal of characterizing the stray-light performance of the immersed gratings with a single number, the total integrated scatter (TIS) excluding ghosts from internal reflections was calculated. Here the contribution from the stray-light background and ghosts were calculated separately and added. For the ghosts the effect of aperture sizes either larger or smaller than the ghost sizes was taken into account and the energy renormalized. The stray-light background was taken from a fit of the background in the spectral off-axis stray-light measurement. The resulting BRDF function was integrated over the complete scattering hemisphere. As a result, a TIS contribution of 0.02% of the ghosts and 0.18% of

the background was estimated, leading to a TIS of 0.2% excluding ghosts from internal reflections. The highest uncertainties in the TIS estimation are due to: a) uncertainties of the use of the scatterometer setup in a new wavelength range (a calibration was done at high signal levels with a Lambertian scatterer, but no reference for low signal levels was available); b) the estimation of the stray-light background assuming a radially symmetric distribution and taking only the data set along one axis. The lower BRDF levels along the spatial axis indicate that the stray light distribution is not radially symmetric and instead decreases towards to spatial axis. No ghosts with a relative intensity of above $10^{-4}$ were found.

### 4.2 Efficiency and polarization

The immersed-grating efficiency has been measured with a photospectrometer over the complete operational spectral range for two polarizations. The results of the efficiency measurements on the SWIR-3 Bread Board Model (BBM) can be seen in Figure 15 and Figure 16. In the efficiency measurement it is essential that all reflected light for each wavelength hits the detector, which includes an integrating sphere. This was achieved by changing the detector angle in fixed steps and by measuring the intensity at each step while scanning the light wavelength over the full spectral range for both polarizations. Afterwards, the data for the different detector positions are overlapped and for each wavelength, the maximum value is taken. This produces the polarized efficiency over the complete spectral range. The average efficiency is calculated by taking the average of the TE and TM polarization data. The polarization sensitivity is calculated as

$$\rho = \frac{E_{TE} - E_{TM}}{E_{TE} + E_{TM}} .$$

Figure 15 shows that the average efficiency of the immersed grating is well above the requirement of 55% with an average value of (60.1 ± 0.3)% over the complete wavelength range. For the simulation with the diffraction efficiency modeling software PCGrate (I.I.G., Inc., New York), a standard deviation in the position of the grating lines of 25 nm rms and losses of twice 0.2% for the antireflection coating were assumed. The average efficiency compares well to the simulated behavior but is up to 3% lower than the simulation. The reason for this discrepancy is unclear but has been expected from the experience from previous immersed-grating projects. The polarization sensitivity shown in Figure 16 also compares well to the simulations and is below the requirement of $|\rho| < 0.17$.

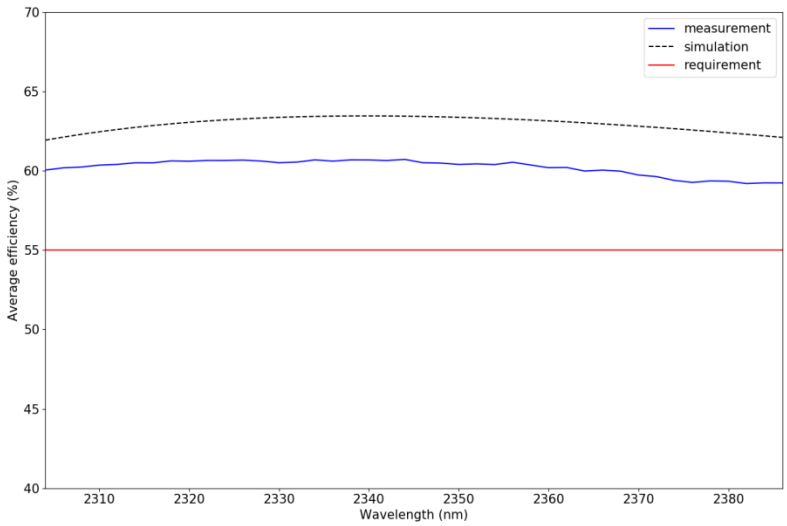


Figure 15. Measured average efficiency as a function of wavelength (blue) compared with the simulation using as-built manufacturing parameters (black dashed) and the requirement (red).

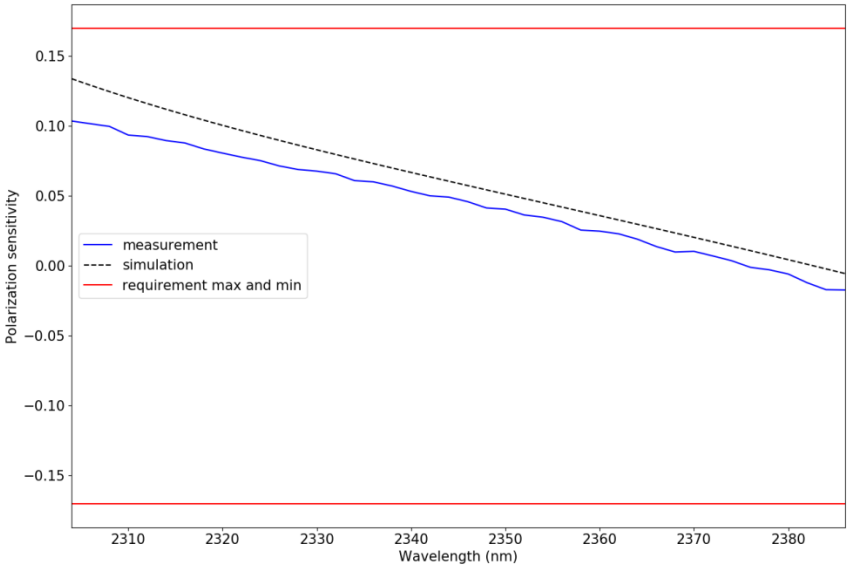


Figure 16. Measured polarization sensitivity as a function of wavelength (blue) compared with the simulation using as-built manufacturing parameters (black dashed) and the requirement (red).

### 4.3 Wavefront error

#### 4.3.1 Reconstruction from surface measurements

The estimation of the wavefront error of the immersed gratings was obtained by separate surface measurements at room temperature. The challenge for the grating surface lies in calculating the wavefront error in operating conditions from autocollimation measurements in Littrow configuration at the outside of the grating. The wavefront error due to a grating has two main contributions: the surface shape error (SSE) of the grating surface and ruling errors, i.e. the deviation of the grating lines from a periodic pattern. For the derivation of the relevant equations, the argumentation by Stroke[10] for the scaling of ruling errors and height variations can be followed. In Figure 17, a schematic diffraction grating with incident (blue) and reflected (red) wavefronts is shown.

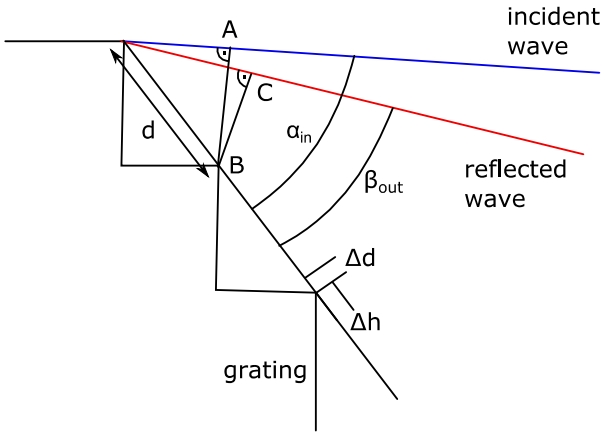


Figure 17. Schematic for derivation of wavefront error equations.

The grating equation can easily be obtained by requiring constructive interference over $\overline{AB} + \overline{BC} = m\lambda$, with wavelength lambda and integer $m$, leading to $d \sin \alpha_{\text{in}} + d \sin \beta_{\text{out}} = m\lambda$. For long spatial correlation lengths, the wavefront error from ruling errors $\text{WFE}_{\text{ruling}}$ and surface shape errors $\text{WFE}_{\text{SSE}}$ are given by

$$\text{WFE}_{\text{ruling}}(\alpha_{\text{in}}, \beta_{\text{out}}) = \Delta d \, (\sin \alpha_{\text{in}} + \sin \beta_{\text{out}}) \,,$$

$$\mathrm{WFE}_{\mathrm{SSE}}(\alpha_{\mathrm{in}}, \beta_{\mathrm{out}}) = \Delta h\ (\cos\alpha_{\mathrm{in}} + \cos\beta_{\mathrm{out}})\ .$$

The scaling laws allow the determination of the wavefront error contributions from autocollimator measurements at two opposing diffraction orders ±*m* at angle $\alpha_{\mathrm{ac}}$ close to $\alpha_{\mathrm{in}}$ and $\beta_{\mathrm{out}}$. The wavefront error contributions from ruling and surface shape errors are then calculated by

$$\mathrm{WFE}_{\mathrm{ruling}}(\alpha_{\mathrm{ac}}) = \frac{\mathrm{WFE}(\alpha_{\mathrm{ac}}) - \mathrm{WFE}(-\alpha_{\mathrm{ac}})}{2},$$

$$\mathrm{WFE}_{\mathrm{SSE}}(\alpha_{\mathrm{ac}}) = \frac{\mathrm{WFE}(\alpha_{\mathrm{ac}}) + \mathrm{WFE}(-\alpha_{\mathrm{ac}})}{2}.$$

This information is then used to calculate the wavefront error for an arbitrary incident angle α and outgoing angle β:

$$\mathrm{WFE}_{\mathrm{grating}}(\alpha, \beta) = \frac{\sin\alpha + \sin\beta}{2\sin\alpha_{\mathrm{ac}}}\ \mathrm{WFE}_{\mathrm{ruling}}(\alpha_{\mathrm{ac}}) + \frac{\cos\alpha + \cos\beta}{2\cos\alpha_{\mathrm{ac}}}\ \mathrm{WFE}_{\mathrm{SSE}}(\alpha_{\mathrm{ac}}).$$

In an immersed grating, this wavefront error is accumulated in a medium of refractive index *n*. Upon leaving the medium, the wavefront error of the grating surface in nm is multiplied by a factor *n*. In addition to the wavefront error transformations, the coordinate system is translated from the grating surface to the exit beam.

The above approach has been used to calculate the wavefront error from the grating surface and subsequently the total wavefront error of the immersed grating taking into account the effect of the entrance surface. The grating surface of the SWIR-3 immersed gratings has been measured at *m*=±5 and *m*=0 with an ESDI Mahr interferometer at 633 nm, where the *m*=0 measurement was used to confirm the scaling law for the surface shape error contribution. The result as calculated for the exit beam can be seen in Figure 18 for the SWIR-3 EM model.

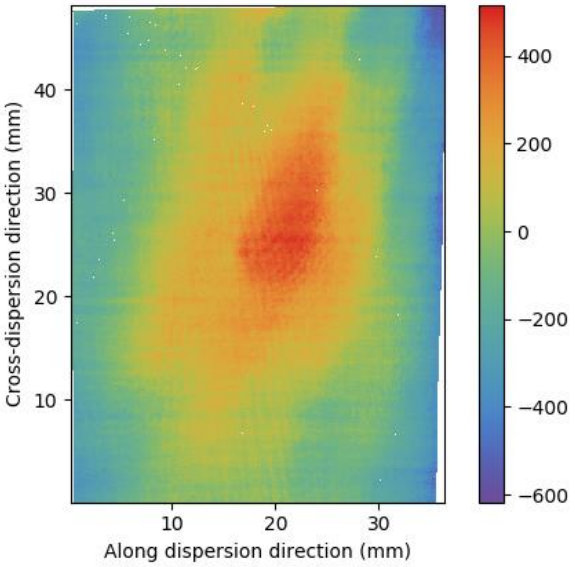


Figure 18. Wavefront error map from the grating surface in the exit beam. The color map scale is in nm

The wavefront error contribution estimated over the complete grating surface is here 180 nm rms. The separate contributions from the surface shape errors and ruling errors are 136 nm rms and 83 nm rms, respectively. The surface shape errors are dominated by the thickness variations of the wafer used for the grating element, leading to wafer thickness variations being the largest contributor to the total immersed grating wavefront error. Prism surfaces were polished with typical surface shape errors of <10 nm rms.

For Sentinel-5, the wavefront error requirement has been formulated as <900 nm rms total wavefront error and <180 nm rms wavefront error after defocus aberration correction over a footprint of 35 mm × 43 mm on the grating area of the SWIR-3 immersed gratings. Including the contribution of passing twice the entrance surface, values of 206 nm rms for the total wavefront error and 136 nm rms for the wavefront error without defocus were found here for the SWIR-3 EM model. For the two other models tested so far, total wavefront error values of 296 nm rms (QM, optically not representative) and 176 nm rms (BBM) were found.

#### 4.3.2 Immersion measurement

A verification of the wavefront error reconstruction from different surface measurements would be best by measurements in immersion with an infrared interferometer. However, no such instrument was available to SRON. As an alternative, an experimental setup was built and tested, based on a Shack-Hartmann sensor and polarization optics. A schematic overview of the setup is shown in Figure 19.

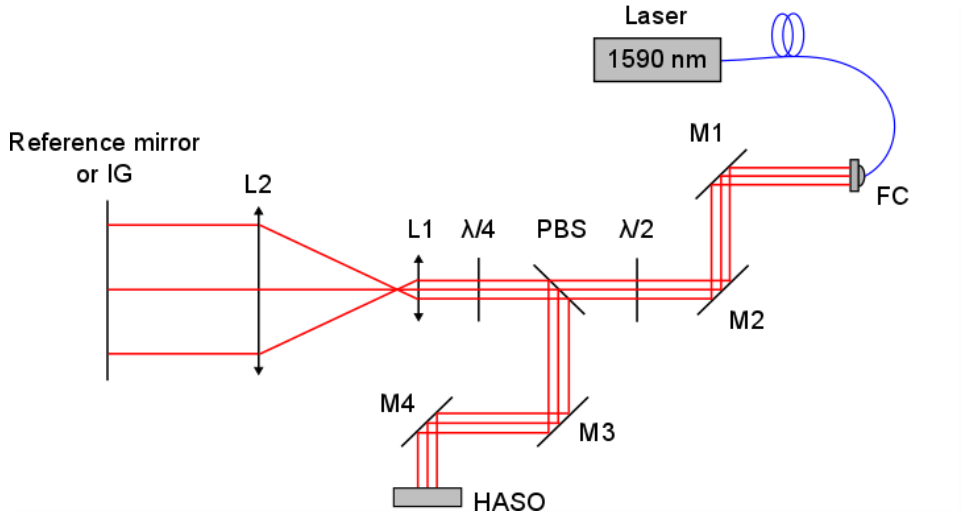


Figure 19. Setup for measurement of immersed grating wavefront error in immersion. The light from a fibered laser at telecom wavelengths passes through a fiber coupler (FC), a half-wave plate (λ/2) and a polarization splitter (PBS). A telescope consisting of two lenses L1 and L2 is used to expand the beam which is reflected by a reference mirror or an immersed grating. By passing a quarter-wave plate twice the polarization is rotated by 90° and reflected by the PBS onto a Shack-Hartmann sensor (HASO).

The principle of the setup relies on expanding a collimated laser beam with a telescope, the reflection from an immersed grating in Littrow configuration, and demagnification with the same telescope to hit a Shack-Hartmann wavefront sensor (HASO4 NIR, Imagine Optic). Polarization optics such as half-wave and quarter-wave plates and a polarization beam splitter are used to control the optical path. Due to the use of off-the-shelf optical components larger aberrations were introduced, especially by the telescope optics. This limited the usable beam diameter to approximately 20 mm when the immersed grating was inserted in the optical path.

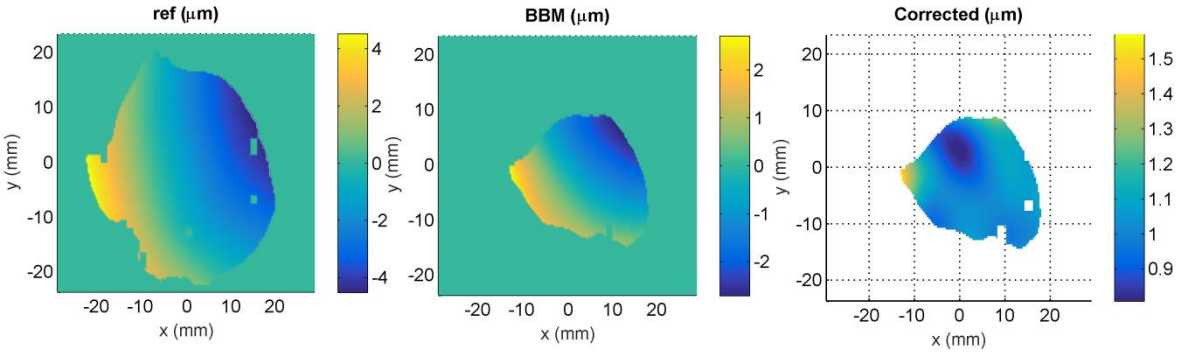


Figure 20. Example of the measured wavefront error in μm, of the reference mirror (left), BBM (middle) and the corrected wavefront (BBM minus reference with tilt correction, right). The final WFE is calculated from the standard deviation for the final corrected wavefront. The wavefront error map is asymmetric due to aberrations in the optical setup which are outside of the dynamic range of the Shack-Hartmann sensor.

Global aberrations of the setup were subtracted with the help of a flat reference mirror instead of the immersed grating and tip/tilt correction. Small alignment errors could cause an additional wavefront error giving rise an unsymmetric uncertainty in the measurement of -40/+20 nm rms.

In Figure 20, the measurement results for the BBM model can be seen. A wavefront error of 110 nm rms was found in an asymmetric region of approximately 20 mm in diameter. This was compared with the results when the wavefront error in a region of similar size was calculated using the calculation from separate surface measurements. With that method, a value of (81 ± 20) nm rms was found. Considering the uncertainty in the immersion measurement of -40/+20 nm rms, the values from the two methods are in good agreement. The performance of the presented setup could be improved by a specially designed beam expansion system using custom optics leading to a better accuracy and larger beam diameter.

## 5. ENVIRONMENTAL TESTING

### 5.1 Vibration and shock

For Sentinel-5, for the first time silicon immersed gratings produced by direct wafer to prism bonding have to survive the conditions of launch into space. The immersed gratings are delivered in a housing, designed by SRON and produced by VDL. The grating assembly is shown in Figure 21 and environmental tests were done with the assembly. The immersed grating is bonded with EC2216 adhesive to six Invar buttons which are in turn bonded with EC2216 to the housing made of Ti-Al6-4V. The housing contains flexures with their compliance towards the thermal center of the system to cope with the thermal expansion differences of silicon and titanium. The total weight was measured to be 429 g.

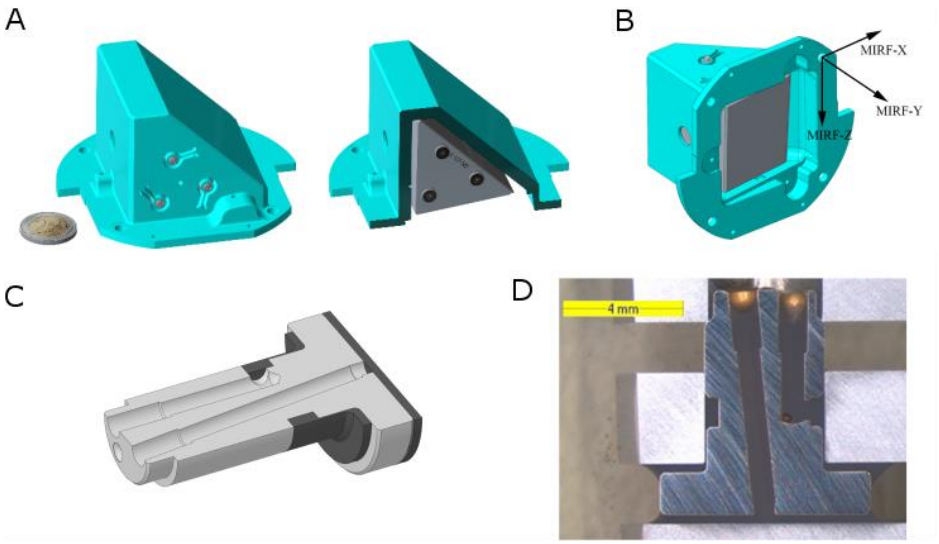


Figure 21. A: CAD model of the SWIR 3 immersed grating and a 2-euro coin for scale comparison. On the right a cross section shows the adhesive connections. B: Mechanical interface reference frame (MIRF). C: CAD model cross section of the Invar button with adhesive channels. D: Cross section of a test sample of the Invar button (blue) with adhesive (black).

Qualification vibration tests were performed on an electrodynamic shaker at ESA-ESTEC. With finite element analysis the first natural frequency of the immersed grating was calculated to be 2380 Hz. Using low-level sine sweeps with a frequency range between 5 and 2000 Hz it was confirmed that the first natural frequency of the QM was indeed above 2000 Hz. Sinusoidal vibration tests were carried out where the acceleration levels were increased from a 1 *g* level at 5 Hz to 44 *g* in MIRF-X and MIRF-Y (see Figure 21) and to 25 *g* in MIRF-Z at 120 Hz with a sweep rate of 2 oct/min. High-level random-vibration tests were also performed with a total 39.8 $g_{rms}$ in MIRF-X, 40.6 $g_{rms}$ in MIRF-Y and 52.6 $g_{rms}$ in MIRF-Z for 120 seconds each.

Qualification shock tests were performed on a shock bench with the grating assembly bolted to a ringing plate. The ringing plate was excited by a pendulum hammer. Three shocks were applied in each direction, 9 in total. The desired shock response spectrum for each shock had its maximum of 500*g* above 2000 Hz and a damping of 5%. The actual applied shock levels varied around the specification in the frequency domain but were within a ±6 dB tolerance margin.

After each vibration test and after shock testing low-level sine sweeps were performed again on the shaker. No change in dynamic behavior was measured. The position and rotation of the prism with respect to the housing were measured before and after vibration plus shock testing with a coordinate measurement machine and did not change. No degradation of the immersed grating including the bonded surface was found.

### 5.2 Thermal vacuum

The optical performance of the immersed grating should not be degraded by thermal cycling and cooldown to the operational temperature of 210 K. Furthermore, rotations with respect to its mechanical interface should be minimal and repeatable. In order to perform thermal vacuum tests on the immersed gratings, a dedicated cryostat setup was built. A schematic overview of the cryostat is shown in Figure 22.

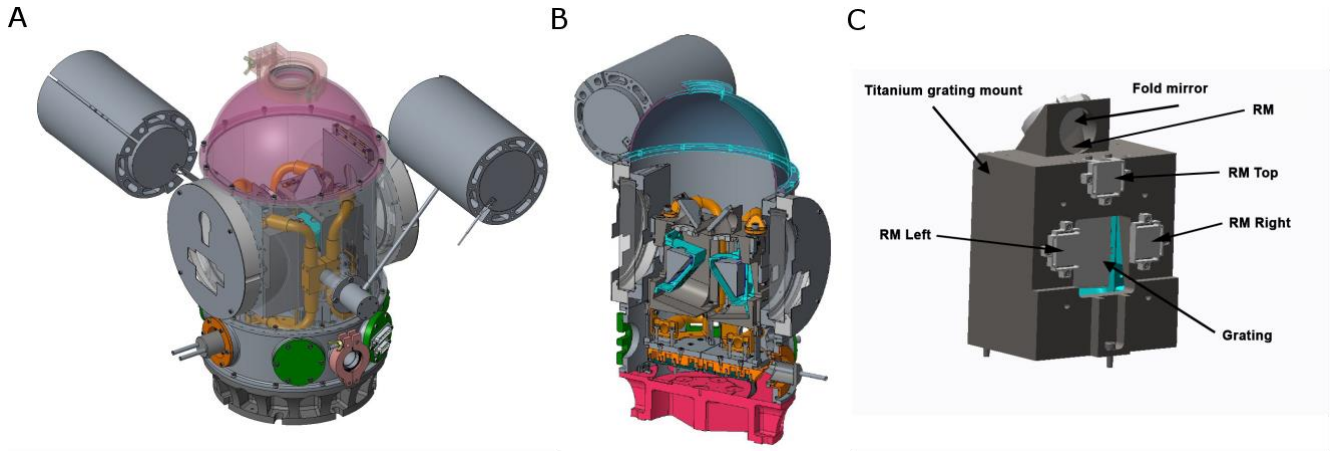


Figure 22. A: Schematic drawing of the test cryostat. The interior is visible showing the titanium mounting block, the thermal strapping and one of the immersed gratings. The setup allows for thermal cycling of two units at a time. B: Cross-section of the cryostat. C: Titanium mounting block with four reference mirrors (RM) and grating. An annular reference mirror RM (not visible in this drawing) supports angular orientation measurements from the top. All mirrors and the mounting structure are made of titanium.

The setup allows the interferometric measurement of the immersed grating surfaces during thermal cycling, as well as rotation measurements with an autocollimator. It further supports the cycling of two immersed gratings in parallel if needed. In Figure 22 also the mounting structure of the immersed grating including four reference mirrors is shown. Both the structure and the mirrors are made of titanium for optical stability and to match the housing. To be able to also determine the angular stability around the MIRF-y axis (by autocollimator measurement), a hole has been added to the top of the grating housing. A reference mirror with annular shape (RM 3th) and a folding mirror have been added to the setup to facilitate this measurement. An entrance window with a large diameter of 100 mm grants sufficient optical access and a wedge angle of 30 arcmin deflects window reflections from the optical path. Thermal cycling relies on two cryocoolers (LSF9320/01, Thales) as well as silicon nitride heaters (GLZ100053, Bach). Thermistors are attached at several positions in the cryostat close to the grating and the heaters in order to control and log the temperature. A control system, which switches between feedforward at steep temperature changes and feedback control when a stable temperature has to be maintained, ensures that temperature profiles can be followed within ±2 K at gradients of up to 0.5 K/min. Several safety measures were taken allowing autonomous operation of the setup, especially to avoid overheating. A cold trap (not shown) between the pump and the cryostat was included in order to minimize contamination by the setup.

An overview of the complete measurement setup including autocollimator and interferometer is presented in Figure 23. The cryostat and optical measurement equipment are placed on a vibration isolated optical table. A folding mirror is used to switch between autocollimator and interferometer measurements. The transmission flat of the interferometer can be aligned with the grating surface to be measured via adjustment screws on the interferometer platform. The autocollimator can be moved to different positions such that always one reference mirror and the surface to be measured are in the field of view in order to determine the relative angle.

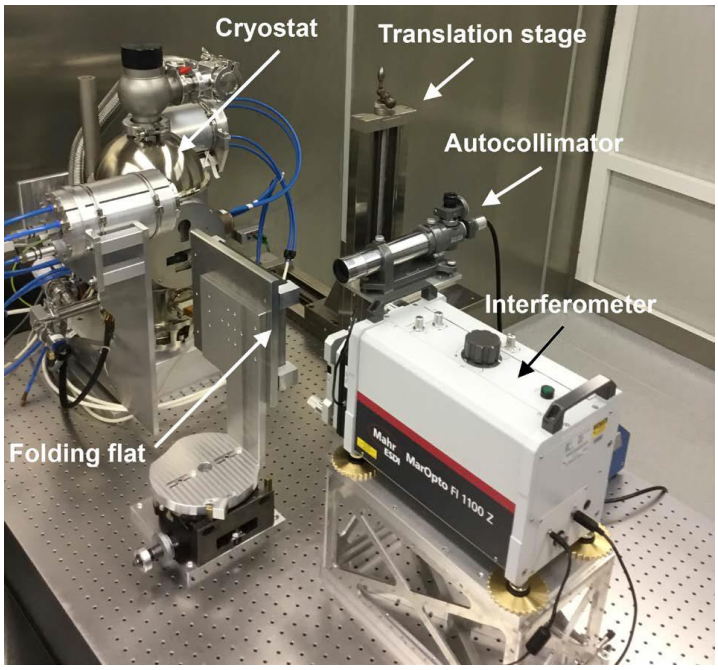


Figure 23. Cryostat setup in class ISO 5 cleanroom including optical measurement equipment. The complete setup is placed on a very stiff vibration isolated optical table. A folding flat is used to switch between interferometer and autocollimator measurements.

Thermal vacuum tests have been performed so far on the BBM, QM and EM SWIR-3 models. Entrance surface-shape measurements were taken with the QM and EM. For the BBM only, the grating surface has been measured after cooldown from room temperature to operational temperature. For this purpose, the grating surface in the housing was kept open, making the model mechanically not representative. Interferometer measurements were performed both for the entrance and grating surfaces at room temperature and operational temperature after dwell times of 4 h in order to allow for thermal stabilization. The cryo-coolers were switched off during measurements to improve the mechanical stability of the setup. The wavefront error of the cryostat entrance window has been evaluated separately by placing a Zerodur mirror instead of an immersed grating in the optical setup. After correction of the effect of the entrance window, no deformation of the immersed grating surfaces were found due to cooldown from room temperature to operational temperature within the accuracy of the setup of 6 nm rms. This result is supported by finite element simulations on the immersed gratings, resulting in maximum deformations of 3.8 nm rms using a conservative elasticity model for the coatings.

Qualification thermal tests have been performed on the QM with 8 cycles in the range between 170 K and 330 K. For the EM, as also intended for the flight models, 4 thermal cycles were performed. Rotations of the immersed grating in its housing were measured both over the operational temperature range from 195 K to 225 K and with respect to room temperature. The measurement results are given in Table 3 using the MIRF coordinate system in Figure 21.

Table 1. Angular variations of the immersed grating in its housing during cooldown from room temperature to operational temperature (210 K) and its stability over the operational temperature range.

| Orientation | Max. change in orientation from 293 K to 210 K (arcsec) | Repeatability from 293 K to 210 K (arcsec) | Stability over operational range (arcsec/K) |
|---|---|---|---|
| $\Theta_x$ | 4.7 ± 1.2 | 1.4 ± 2.2 | 0.05 ± 0.20 |
| $\Theta_y$ | 4.1 ± 1.0 | 3.3 ± 2.8 | 0.08 ± 0.06 |
| $\Theta_z$ | -49.0 ± 1.9 | 1.6 ± 3.0 | 0.49 ± 0.09 |

The thermal vacuum tests showed that at least one cycle is needed to remove pretensions in the grating assembly. Rotations were therefore only measured after the first cycle. The largest rotation of approximately 50 arcseconds from room temperature to operational temperature was found around the z-axis. However, an excellent repeatability of the rotations of less than 2 arcseconds was found, allowing for the precompensation in the design of the spectrometer. In general, in all thermal vacuum tests no degradation of the immersed gratings and their housing as a result of thermal cycling was found.

## 6. CONCLUSIONS

An overview has been provided of the immersed-grating design, manufacturing and optical and environmental testing for the Sentinel-5 mission. The design of the immersed gratings was driven by constraints such as a close to constant dispersion and no additional peaks from other orders or internal reflections within a range of ±10° from the main diffraction peak. For the manufacturing of the immersed gratings, direct contact bonding between a grating-element wafer and a silicon prism was used. Grating elements were produced with UV lithography and KOH etching, resulting in very smooth (<0.5 nm rms roughness) blazed surfaces and dam width variations below 25 nm rms. Details have been given on the bonding with precise control over translation and rotation of the two parts. A rotation accuracy below 100 arcseconds was obtained. Void-free bonds between prisms and grating elements were achieved for all immersed gratings.

For the wavefront error a method has been presented to calculate and characterize the contributions of the grating surface to the immersed-grating wavefront error in operational conditions using Littrow measurements at different orders, which could be used for the characterization of transmission and reflection gratings in general. Values of 200 nm rms wavefront error for the SWIR-3 immersed gratings were obtained. The method using separate surface measurements was verified with an experimental Shack-Hartmann setup allowing immersion infrared measurements with a beam diameter of 20 mm and an accuracy of −20/+45 nm.

The approach to measure the stray light of the immersed gratings has been shown, with a discussion of the challenging characterization of an anisotropic distribution with a limited number of line scans over the stray-light hemisphere. The total integrated scatter over the complete stray-light hemisphere was estimated to be 0.2%. This was dominated by the stray-light background, which was calculated from the spherical integration of a measurement close to the dispersion axis of the immersed grating. In reality, the total integrated scatter was likely to be lower as indicated by lower BRDF values on the spatial axis of the immersed grating, pointing towards a non-rotational symmetric background. No ghosts with a relative intensity of larger than $10^{-4}$ were found.

An average efficiency of 60% and a maximum polarization sensitivity of 0.11 were determined, close to the expected values from simulations. After the integration of the immersed gratings into their housings, vibration, shock and thermal vacuum tests were passed and no degradation of the immersed-grating performance was found. The prism to grating element bond was therefore shown to survive the tested conditions of launch and thermal cycling.

The immersed gratings comply with the requirements for the Sentinel-5 mission. However, future immersed gratings for astronomy, for example for the Extremely Large Telescope,[11] might require a lower wavefront error. The largest contribution to the immersed grating wavefront error is due to wafer-thickness variations. This may be corrected by computer polishing techniques such as magnetorheological finishing (MRF) or ion beam figuring. Our initial attempts for the correction of the wafer-thickness variations with MRF failed however, because of mid-spatial frequency surface shape errors on the length scale of the polishing slurry beam diameter, which posed difficulties in the grating-element manufacturing and bonding. The second largest wavefront error contribution from long spatial correlation length ruling errors could be reduced by switching to a different grating patterning strategy before KOH etching. A possibility here would be electron beam writing where very low ruling errors as well as low ghost intensities have already been demonstrated[12,13]. Surface shape errors on the grating and entrance prism surfaces could similarly be reduced with computer polishing techniques.

The stray-light evaluation of the immersed gratings was limited to a set of line scans on the stray-light hemisphere, which made the characterization of the anisotropic distribution difficult. This points towards the need of high dynamic

range 3D scatterometer setups in the SWIR and IR. The contribution of surface roughness to the stray-light background was expected to be very low due to the KOH etching, but was measured to be higher, possibly due to the coatings. Stray-light measurements should be performed on samples after every stage to look for mitigating actions.

The presented SWIR wavefront-error measurement setup is an interesting alternative when no infrared interferometer but only a Shack-Hartmann sensor is available. For the use as a metrological tool the design and performance of the beam expansion and polarization optics would need to be improved.

## ACKNOWLEDGEMENTS

We would like to thank the team of the optical measurement lab at ESA-ESTEC for the performance of the challenging stray-light measurements.

## REFERENCES

[1] Leitner, A., "The life and work of Joseph Fraunhofer (1787-1826)," Am. J. Phys. 43, 59-68 (1975).
[2] Marsh, J. P., Mar, D. J., and Jaffe, D. T., "Production and evaluation of silicon immersion gratings for infrared astronomy," Appl. Opt. 46, 3400-3416 (2007).
[3] Kuzmenko, P. J., Davis, P. J., Little, S. L., Little, L. M, Bixler, J. V., "High efficiency germanium immersion gratings," Proc. SPIE 6273, Optomechanical Technologies for Astronomy, 62733T (2006).
[4] Sukegawa, T., Suzuki, T., Kitamura, T. "Astronomical large Ge immersion grating by Canon," Proc. SPIE 9912, Advances in Optical and Mechanical Technologies for Telescopes and Instrumentation II, 99122V (2016).
[5] Veefkind J. P., Aben, I., McMullan, K., et al., "TROPOMI on the ESA Sentinel-5 Precursor: A GMES mission for global observations of the atmospheric composition for climate, air quality and ozone layer applications," Remote Sensing of Environment 120, 70-83 (2012).
[6] Amerongen, A. H. van, Visser, H., Vink, R. J. P., Coppens, T., Hoogeveen, R. W. M., "Development of immersed diffraction grating for the TROPOMI-SWIR spectrometer," Proc. SPIE 7826, Sensors, Systems, and Next-Generation Satellites XIV, 78261D (2010).
[7] Amerongen, A. van, Krol, H., Grèzes-Besset, C., Coppens, T., Bhatti, I., Lobb, D., Hardenbol, B., Hoogeveen, R., "State of the art in silicon immersed gratings for space," Proc. SPIE 10564, International Conference on Space Optics — ICSO 2012, 105642R (2017).
[8] Boni, A., Taiti, A., Bini, A., Pasqui, C., "Sentinel-5 short-wave infrared spectrometer optical design," Proc. SPIE 10690, Optical Design and Engineering VII, 106901J (2018).
[9] Rodenhuis, M., Tol, P. J. J., Coppens, T. H. M., Laubert, P. P., and Amerongen, A. H. van, "Performance of silicon immersed gratings: measurement, analysis, and modeling," Proc. SPIE 9626, 1M, (2015).
[10] Stroke, G. W., "Ruling, Testing and Use of Optical Gratings for High-Resolution Spectroscopy" Progress in Optics 2, 1-72 (1963).
[11] Amerongen, A. H. van, Agocs, T., Brug, H. van, Nieuwland, G., Venema, L., Hoogeveen, R. W. M. "Development of silicon immersed grating for METIS on E-ELT," Proc. SPIE 8450, Modern Technologies in Space- and Ground-based Telescopes and Instrumentation II, 84502T (2012).
[12] Zeitner, U.D., Oliva, M., Fuchs, F. et al., "High performance diffraction gratings made by e-beam lithography," Appl. Phys. A 109: 789 (2012).
[13] Heusinger, M., Banasch, M., and Zeitner, U. D., "Rowland ghost suppression in high efficiency spectrometer gratings fabricated by e-beam lithography," Opt. Express **25**, 6182-6191 (2017).